



Stable High-Capacity Lithium Ion Battery Anodes Produced by Supersonic Spray Deposition of Hematite Nanoparticles and Self-Healing Reduced Graphene Oxide



Jong-Gun Lee^{a,1}, Bhavana N. Joshi^{a,1}, Jong-Hyuk Lee^a, Tae-Gun Kim^a, Do-Yeon Kim^a, Salem S. Al-Deyab^b, Il Won Seong^c, Mark T. Swihart^d, Woo Young Yoon^{c,*}, Sam S. Yoon^{a,*}

^a School of Mechanical Engineering, Korea University, Seoul 136-713, Republic of Korea

^b Petrochemical Research Chair, Department of Chemistry, King Saud University, Riyadh 11451, Saudi Arabia

^c Department of Materials Science & Engineering, Korea University, Seoul 02841, Republic of Korea

^d Department of Chemical & Biological Engineering, University at Buffalo, The State University of New York, Buffalo, New York, 14260-4200, United States

ARTICLE INFO

Article history:

Received 17 August 2016

Received in revised form 13 January 2017

Accepted 18 January 2017

Available online 20 January 2017

Keywords:

Supersonic spray coating

Hematite

Iron oxide

Reduced graphene oxide

Lithium ion battery

Anode

ABSTRACT

Hematite (Fe_2O_3) nanoparticles and reduced graphene oxide (rGO) were supersonically sprayed onto copper current collectors to create high-performance, binder-free lithium ion battery (LIB) electrodes. Supersonic spray deposition is rapid, low-cost, and suitable for large-scale production. Supersonic impact of rGO sheets and Fe_2O_3 nanoparticles on the substrate produces compacted nanocomposite films with short diffusion lengths for Li^+ ions. This structure produces high reversible capacity and markedly improved capacity retention over many cycles. Decomposition of lithium oxide generated during cycling activates the solid electrolyte interface layer, contributing to high capacity retention. The optimal composition ratio of rGO to Fe_2O_3 was 9.1 wt.%, which produced a reversible capacity of 1242 mAh g^{-1} after $N = 305$ cycles at a current density of 1000 mA g^{-1} (1C).

© 2017 Elsevier Ltd. All rights reserved.

1. Introduction

Lithium ion batteries (LIB) are an essential component of portable electronic devices and are gaining importance in electric and hybrid electric vehicles [1]. Despite these successes, new applications demand higher power density combined with stable performance over many charge-discharge cycles to meet ever-growing demands for portable energy storage [2,3]. Recent research has stressed the development of new and hybrid anode and cathode materials that can provide high capacity and retain their capacity over many charge-discharge cycles [4].

Metal oxides in combination with carbon have demonstrated high capacity as anode materials [5]. Transition metal oxides (TMOs), such as Co_3O_4 , CoO , NiO , CuO_x , Fe_2O_3 , and Fe_3O_4 , have shown promise as LIB anode materials [6]. They are classified as conversion materials, because their reaction with lithium ions involves reduction of the transition metal, *i.e.* conversion of the

metal oxide to metal. These materials can exhibit gravimetric capacities that are 2–3 times that of graphite (372 mAh g^{-1}) [7]. However, when used alone, their performance typically deteriorates after a few charge-discharge cycles. Moreover, alone, these TMOs lack electrical conductivity required for electron extraction from the anode. To overcome this limitation, TMOs have often been combined with carbon materials (carbon black, carbon nanotubes, or graphene), which provide electrical conductivity and mechanical support while accommodating the volume changes of TMO nanostructures that occur during charge-discharge cycling [8].

Iron oxide (Fe_2O_3) is a low cost, environmentally friendly TMO with a theoretical specific capacity of 1007 mAh g^{-1} as a LIB anode [9]. During insertion and extraction of Li^+ , Fe_2O_3 undergoes reduction to form iron particles, which ultimately leads to degradation of anode performance. As is typical of TMO anodes, Fe_2O_3 suffers from “capacity fading” due to the phase-change and volume change that occurs during Li^+ insertion and extraction. These processes can also lead to detachment of the coating layer from the current collector [10]. Moreover, diffusion of Li^+ ions in Fe_2O_3 is slow, and electron transport in Fe_2O_3 is poor. These factors limit the rate capability of Fe_2O_3 anodes. To circumvent these issues, various types of Fe_2O_3 nanostructures have been explored in the form of nanoparticles, nanorods, and nanotubes [11]. These

* Corresponding authors.

E-mail addresses: wyyoon@korea.ac.kr (W.Y. Yoon), skymoon@korea.ac.kr (S.S. Yoon).

¹ These authors have contributed equally.

reduce the transport distances within Fe_2O_3 for both Li^+ ions and electrons and can better accommodate volume and phase changes compared to larger structures. However, the high surface area of the nanostructures themselves may promote decomposition of the electrolyte when Li-ions are attached to them. After the surface reaction, Li^+ ions are permanently converted into LiO_2 , which reduces the quantity of Li^+ ions available to participate in the charge-discharge cycles, again resulting in capacity fading [12].

Addition of carbon materials such as carbon black (CB), carbon nanotubes (CNT), graphene, or reduced graphene oxide (rGO), to Fe_2O_3 not only helps to accommodate volume and phase changes, but also significantly improves the overall electrical conductivity of the anode. Both of these factors contribute to improved long-term stability and performance. However, most fabrication methods employ binders to produce Fe_2O_3 composites with carbon materials. Previously reported methods include sol gel [13,14], solvothermal [15], hydrothermal [16,17] electrospray [18], and spray pyrolysis [19] techniques. Binders used in these methods reduce capacity and may impede electron and ion transport. Moreover, these production methods are relatively complex and involve multiple steps, which increases production cost. A simple, single-step, “binder-free” approach to the fabrication of Fe_2O_3 -carbon composites would thus be very valuable.

Supersonic cold spraying directly deposits Fe_2O_3 nanoparticles and rGO sheets simultaneously without the use of any binders. By simply sweeping a nozzle across a substrate, a film with superior adhesion and uniformity can be produced very rapidly [20]. The supersonic impact between the materials being deposited and the substrate produces excellent adhesion of the deposited film. Further compaction and densification of the deposited materials by subsequently impacted material enhances the cohesion between rGO and Fe_2O_3 . Supersonic cold spraying of rGO has been shown to produce a “self-healing” effect during the supersonic impact that also induces stretching of the rGO flakes. This may contribute to the enhanced performance of the resulting rGO films [21]. With the proposed supersonic cold spray deposition process, entanglement between the Fe_2O_3 nanoparticles and rGO sheets prevents agglomeration of the nanoparticles without the addition of binders [2,22,23].

In this study, we demonstrate fabrication of rGO- Fe_2O_3 LIB electrodes via supersonic cold spraying. The electrodes were characterized by scanning electron microscopy (SEM), transmission electron microscopy (TEM), X-ray diffraction (XRD), and Raman spectroscopy. The rGO to Fe_2O_3 ratio was optimized. Galvanostatic charge-discharge curves and specific capacity were compared for varied rGO content to elucidate the detailed mechanism of the rGO contribution to enhanced LIB anode performance.

2. Experimental

2.1. rGO- Fe_2O_3 composite

Fig. 1 shows a schematic illustration of the cold spray coating process. The apparatus includes an air tank, in-line heater, supersonic nozzle, x-y stage, atomizer, and syringe pump. The precursor dispersion consisted of 2.75 g of Fe_2O_3 (>99%, Sigma-Aldrich) and up to 0.25 g of rGO (N002-PDR, Angstrom Materials), dispersed in 40 mL of dimethylformamide (DMF, Reagent Duksan, Korea). 0.3 mL of polyacrylonitrile (PAN) solution in DMF (8 wt%; Sigma-Aldrich, average M_w 150,000) was added to the rGO/ Fe_2O_3 dispersion to improve its colloidal stability. Representative TEM images and SAED patterns of rGO and Fe_2O_3 are shown in Fig. S1 of the supplementary. The Fe_2O_3 and rGO content and ratios used in this study are summarized in Table 1. Air, heated to 250 °C and compressed to 4 bar, was accelerated through a converging-

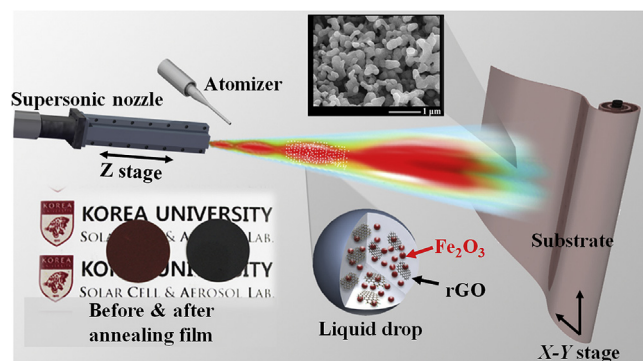


Fig. 1. Schematic illustration of the cold spray coating process.

Table 1
Precursor composition.

Case No.	rGO: Fe_2O_3 [g]	rGO/ Fe_2O_3 [%]
1	0.00: 2.75	0
2	0.05: 2.75	1.8
3	0.15: 2.75	5.5
4	0.25: 2.75	9.1

diverging nozzle to supersonic velocity. The Fe_2O_3 /rGO precursor dispersion was supplied at a flow rate of 1.5 mL min^{-1} via a syringe pump. The precursor was atomized by the supersonic gas stream, and then impacted the substrate at high speed. The mechanism and apparatus have been described in greater detail in our prior reports [24–27].

Before use as anodes, the cold-sprayed films were annealed in Ar at 700 °C for 120 min. The temperature was increased from room temperature to 700 °C at a rate of 3 °C min^{-1} . The annealing process carbonized the small amount of PAN (<1% of the Fe_2O_3 in the precursor dispersion). The color of the Fe_2O_3 /rGO film changed from red to black after the annealing process, as shown in Fig. 1.

2.2. Electrochemical tests

The samples were punched into circular electrodes (14 mm diameter) and CR2032 coin-type half-cells were prepared for electrochemical testing. A Li sheet was used as a reference electrode, and a microporous polymer separator (Celgard 2400; Celgard, Chungbuk, South Korea) was placed between the two electrodes. The cell used a liquid electrolyte composed of 1 M LiPF_6 in a solvent mixture of ethylene carbonate (EC), dimethylcarbonate (DMC), and ethyl methyl carbonate (EMC) (1:1:1 by volume) (PuriEL, Soulbrain, Seongnam, South Korea). The average thickness of Fe_2O_3 /rGO on the Cu foil was estimated to be 2.01 μm based upon the cross sectional TEM image in Fig. S2. The areal density of the electrode was 1.3 mg/cm^2 . Galvanostatic discharge/charge curves were measured between 0.01 and 3 V at 25 °C using a WBCS3000 battery cycler system (WonATech, Seoul, South Korea). The cells were initially subjected to rate tests at different current densities (10 cycles each at 100 mA g^{-1} , 200 mA g^{-1} , 500 mA g^{-1} , and 1000 mA g^{-1}), followed by a 60-cycle test at 100 mA g^{-1} . Long-term cycling tests were conducted at high current density (1000 mA g^{-1}).

2.3. Characterization

Crystallinity of precursors and films was characterized by X-ray diffraction (XRD, SmartLab, Rigaku). Surface morphology and elemental mapping analyses were performed using a field

emission scanning electron microscope (FE-SEM, S-5000, Hitachi, Ltd.) and a transmission electron microscope (TEM, JEM 2100F, JEOL Inc.). The TEM sample was prepared by the focused ion beam (FIB, 5 nA, LYRA3 XMH, TESCAN) technique, which cut the film to produce the cross-sectional image. A confocal Raman spectrometer (Jasco, NRS-3100) was used to analyze the rGO in the cold sprayed films. X-ray photoelectron spectroscopy (XPS, Theta Probe Base System, Thermo Fisher Scientific Co.) measurements were conducted to evaluate the chemical states of the elements in the films and the overall elemental composition of the film surface.

3. Results and Discussion

3.1. Material properties

Typical FE-SEM images of annealed films of pure Fe_2O_3 and $\text{Fe}_2\text{O}_3/\text{rGO}$ composites are presented in Fig. 2. The Fe_2O_3 particles have elongated shapes and coat the Cu substrate, as shown in Fig. 2(a). The FE-SEM images of the nanocomposites shown in Figs. 2(b), (c), and (d) demonstrate the intimate intermixing of Fe_2O_3 particles and rGO nanosheets in the films. At low rGO concentration (Case 2), the Fe_2O_3 particles and rGO are randomly distributed. In Case 3, the Fe_2O_3 particles appear to be supported by rGO nanosheets, increasing the surface area of the electrode, which is expected to enhance the specific capacity. At high rGO concentration, the Fe_2O_3 particles are wrapped in the rGO sheets and it appears that Fe_2O_3 is uniformly dispersed under a cushion of rGO nanosheets (Case 4) with lower surface area and Fe_2O_3 exposure. Further, TEM and energy-dispersive X-ray spectroscopy (EDS) elemental mapping images of films are shown in Fig. S3, where the samples were prepared via the focused ion beam technique in order to acquire the cross-sectional image. The TEM image in Fig. S3 shows that rGO and the Fe_2O_3 particles are intimately combined. The Fe_2O_3 particles (~ 200 nm size) were covered with rGO in the $\text{Fe}_2\text{O}_3/\text{rGO}$ composite film.

The XRD patterns of Fe_2O_3 powder, a cold sprayed $\text{Fe}_2\text{O}_3/\text{rGO}$ film, and an annealed $\text{Fe}_2\text{O}_3/\text{rGO}$ composite film are shown in Fig. 3. The obvious diffraction peaks of the as-deposited $\text{Fe}_2\text{O}_3/\text{rGO}$

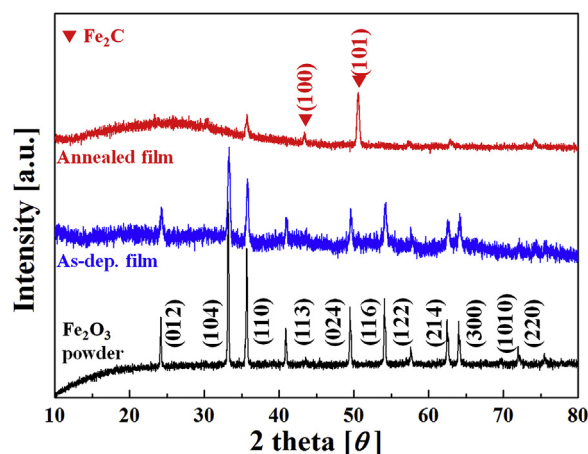


Fig. 3. XRD patterns of Fe_2O_3 powder, as-deposited $\text{Fe}_2\text{O}_3/\text{rGO}$ composite film (Case 3), and annealed $\text{Fe}_2\text{O}_3/\text{rGO}$ composite film.

composite match well with those of the Fe_2O_3 powder, suggesting no major change during cold spraying. The peaks at 2θ values of 24.2° (012), 33.2° (104), 35.7° (110), 40.9° (113), 49.5° (024), 54.0° (116), 57.6° (122), 62.5° (214), 64.1° (300), 72.0° (1010), and 75.5° (220) are indexed to the hematite phase ($\alpha\text{-Fe}_2\text{O}_3$, JCPDS No. 79-0007) [22], consistent with the SAED pattern of Fe_2O_3 particles before their deposition (Fig. S1(b)). However, after annealing the $\text{Fe}_2\text{O}_3/\text{rGO}$ sample under argon gas, the intensity of the Fe_2O_3 peaks decreased. A new peak appeared at $2\theta = 51.5^\circ$ due to formation of Fe_2C , matching JCPDS file 36-1249. The presence of the Fe_2C phase was also evident from the SAED pattern as shown in Fig. S4 along with diffraction rings of Fe_2O_3 and rGO.

Carbon materials are often characterized by Raman analysis because of their unique Raman signatures. The Raman spectra for Case 3 and Case 4, presented in Fig. 4, show peaks at $\sim 1330\text{ cm}^{-1}$ (D band) and $\sim 1585\text{ cm}^{-1}$ (G band) associated with disordered carbon and graphitic carbon, respectively. In carbon materials, the D band is derived from defects in the carbon material, related to

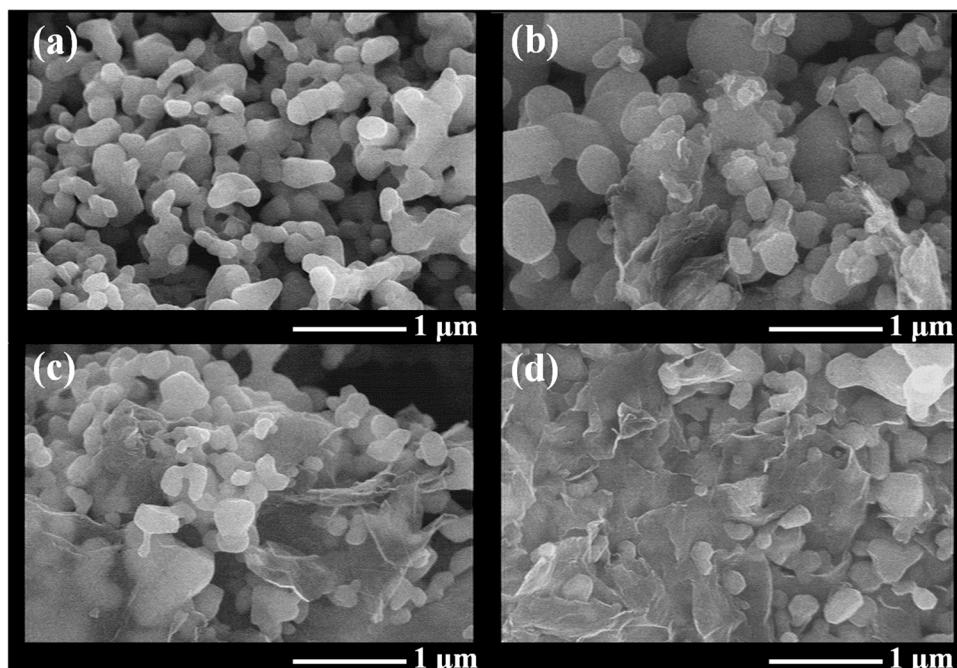


Fig. 2. SEM images of annealed films of varying rGO/ Fe_2O_3 ratios. (a) Pure Fe_2O_3 (Case 1), (b) rGO/ $\text{Fe}_2\text{O}_3 = 1.8\%$ (Case 2), (c) rGO/ $\text{Fe}_2\text{O}_3 = 5.5\%$ (Case 3), and (d) rGO/ $\text{Fe}_2\text{O}_3 = 9.1\%$ (Case 4) after annealing.

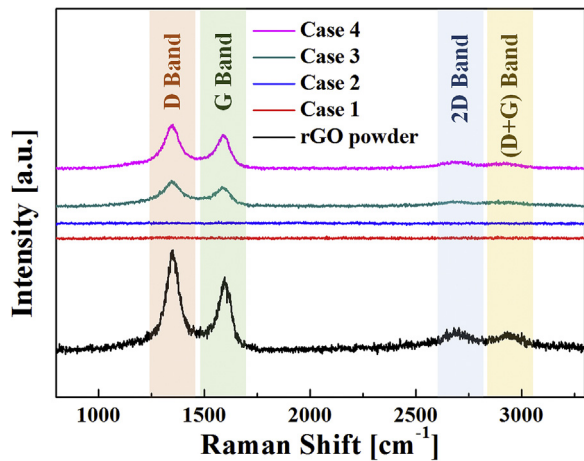


Fig. 4. Raman spectra of $\text{Fe}_2\text{O}_3/\text{rGO}$ composites.

inter-valley scattering, and the G band originates from the doubly degenerate zone center E_{2g} mode. In contrast, the 2D peak arises from second-order zone boundary phonons[28]. Peaks related to the 2D and D+G bands were also observed at about 2700 and 2900 cm^{-1} , respectively[22]. Initially, the intensity ratio ($r = I_D/I_G$) of the rGO powder was 1.35, whereas the ratio was lowered to 1.1 in **Cases 3** and **4**. This change indicates that the number of defects in rGO decreased, suggesting that rGO was healed during deposition and annealing. Such self-healing and stretching of rGO during cold spraying[21] can efficiently wrap Fe_2O_3 and improve the overall electrode performance. **Case 1** corresponds to the pure Fe_2O_3 sample; hence, it is graphene-free. The absence of clear graphene

peaks in **Case 2** may be due to the very low graphene concentration.

XPS analysis was performed to identify the oxidation states and chemical composition of the $\text{Fe}_2\text{O}_3/\text{rGO}$ composite; the results are presented in Fig. 5. The survey spectrum (Fig. 5(a)) confirms the presence of Fe, O, and C with peaks located at 974.5 (O), 933.7, 784.7 (Fe), 724.5, 710.8 (Fe 2p), 530 (O 1s), 284.5 (C 1s), 93.5 (Fe 3s), and 55.7 eV (Fe 3p), respectively. The atomic concentrations of elements determined by XPS is C $\sim 77.1\%$, O $\sim 15.5\%$ and Fe 2p $\sim 7.4\%$. The deconvoluted C 1s XPS data are presented in Fig. 5(b), showing five evident peaks at 284, 285, 286.2, 288 and 291 eV. The peak at 284 eV can be assigned to the sp^2 C—C bonding of rGO. This peak also includes a contribution from iron carbide (Fe-C). The peaks at 285, 286.2, 288 and 291 eV are ascribed to the C—C (sp^3), C—O (alkoxy), C=O (carbonyl), and COOH bonds, respectively [29,30]. Compared with the C—C peak, the lower intensity carbon-oxygen peaks suggest that most of the oxygen-containing functional groups were removed during annealing.

Fig. 5(c) presents the high-resolution Fe 2p spectrum, which shows two obvious peaks of Fe $2p_{3/2}$ and Fe $2p_{1/2}$ at 710.45 eV and 724.41 eV, respectively. The separation of the 2p doublet is ~ 14.0 eV. This finding implies the presence of Fe(III), which is consistent with the Fe_2O_3 phase[31]. In addition, two shake-up satellites with binding energies of 717.49 and 732.31 eV were also clearly observed[32]. The high-resolution O 1s spectrum (Fig. 5(d)) could be deconvoluted into three contributions. The peak at 529.7 eV corresponds to Fe—O in Fe_2O_3 . The peak at 532 eV is attributed to surface species, including hydroxyls, chemisorbed oxygen, and water on the surface of $\text{Fe}_2\text{O}_3/\text{rGO}$.

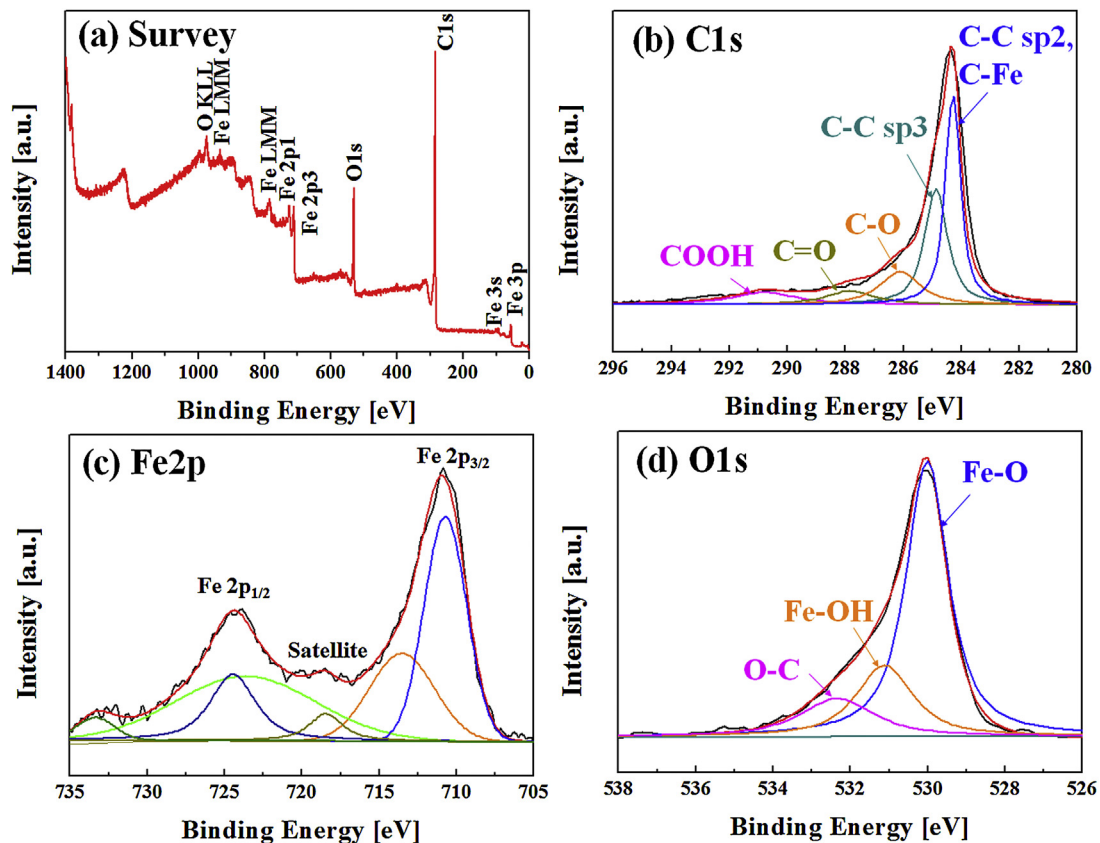


Fig. 5. XPS analysis of Case 3.

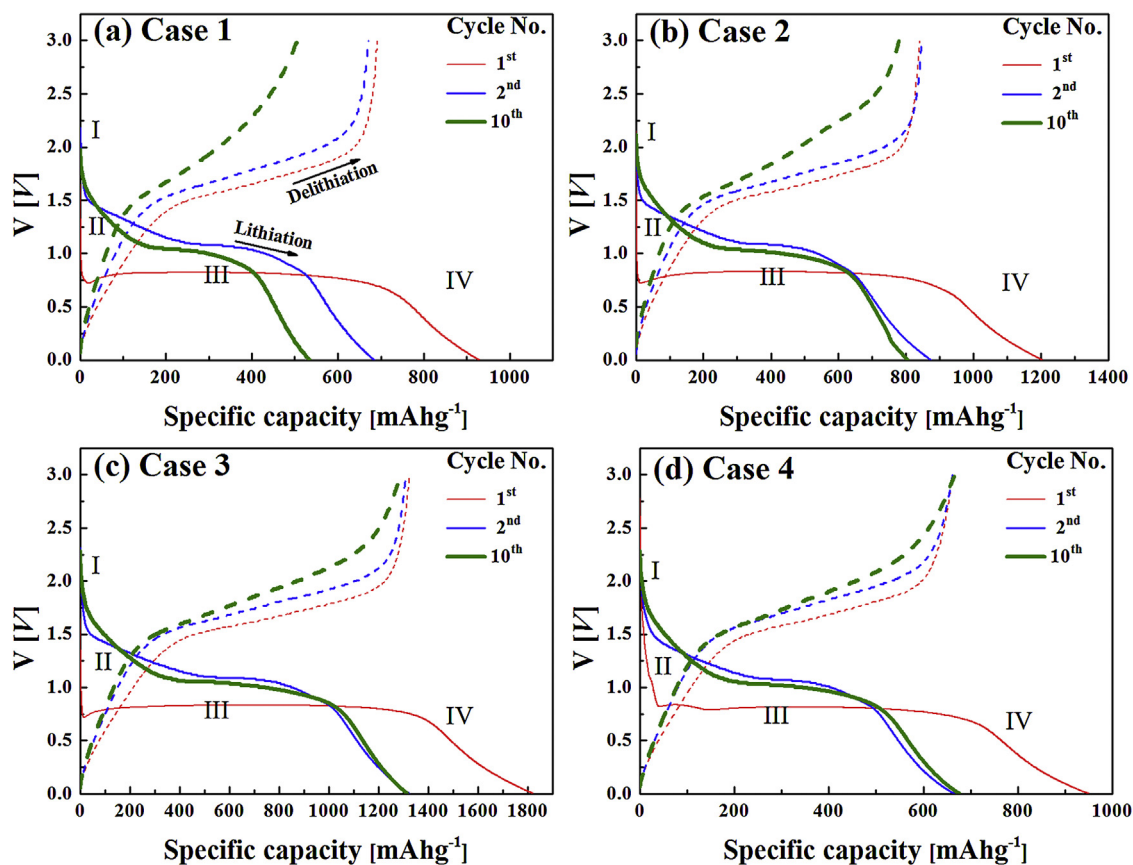


Fig. 6. Discharge/charge curves for (a) Case 1, (b) Case 2, (c) Case 3, and (d) Case 4 at 100 mA g^{-1} .

3.2. Anode performance

Fig. 6 shows galvanostatic charge–discharge (or delithiation–lithiation) curves at a current density of 100 mA g^{-1} for cycle number $N=1, 2$, and 10 . The results shown in Fig. 6(a–d) correspond to rGO concentrations of 0, 1.8, 5.5, and 9.1 wt.%, respectively. For the lithiation process, distinct regions labeled I, II, III, and IV were observed. Region I corresponds to the steepest drop in voltage and region II corresponds to a moderate voltage drop. Region III is the flat or plateau region and Region IV is the final drop to zero voltage. The sharp drop in regions I and II corresponds to lithium insertion from 3.0 to 0.8 V. Region III is characterized by a long plateau near 0.8 V, corresponding to reduction of Fe^{3+} to Fe^0 [23]. Region IV corresponds to continuation of the discharge reaction down to the lower cutoff of 0.01 V for the total first discharge cycle [10]. The specific capacity was calculated based upon the combined mass of $\text{Fe}_2\text{O}_3/\text{rGO}$ present in the composite. The discharge capacities for pure Fe_2O_3 without rGO were 920, 640, and 530 mAh g^{-1} for $N=1, 2$, and 10 , respectively (Fig. 6a). The capacity was significantly enhanced to 1820, 1300, and 1300 mAh g^{-1} when 5.5 wt.% rGO was incorporated into the film (Fig. 6c). Note that the theoretical capacity of Fe_2O_3 is 1007 mAh g^{-1} based on the reduction of Fe^{3+} to Fe^0 by uptake of 6 Li^+ per Fe_2O_3 formula unit. For $N=1$, the highest capacity of 1820 mAh g^{-1} is substantially greater than this theoretical value. The excess capacity can be explained by three possible mechanisms. First, the large surface area facilitates complete reduction of Fe^{3+} to Fe^0 [33]. Second, low voltage decomposition of the electrolyte causes the capacity to increase due to subsequent formation of a solid electrolyte interphase (SEI) layer [10]. Third, the $\text{Fe}_2\text{O}_3/\text{Fe}_2\text{C}$ heterogeneous phase formation can also increase the capacity via interfacial lithium storage [2]. In Case 4, the rGO may

completely cover the Fe_2O_3 particles, as shown in the SEM and TEM images. This limits the reduction of Fe^{3+} to Fe^0 , ultimately leading to lower specific capacity. For $N \geq 2$, region II was distinctively apparent, marking the voltage range from 1.5 to 1.2 V. This distinct region II at $N \geq 2$ is attributed to the structural modifications of Fe_2O_3 after the first cycle ($N=1$) of lithium insertion and extraction [12].

As shown in Fig. 6(a), the lithiation lines for $N=2$ and 10 do not overlap when Fe_2O_3 is used alone. However, when rGO is included in the film, these curves nearly overlap (Fig. 6b–d), demonstrating rapid stabilization of the battery performance as a result of self-healing of rGO [21]. A similar trend was also observed in the “delithiation” lines, with the curves remaining closer together for higher rGO concentration. The delithiation lines presented in Fig. 6(a) deviate significantly. However, with increasing rGO concentration, the distance between these lines closes, the pattern of which indicates improved stability.

The specific capacity of the $\text{rGO-Fe}_2\text{O}_3$ electrodes was investigated at various current loadings of 100, 200, 500, and 1000 mA g^{-1} for up to 100 cycles, as shown in Fig. 7. The specific capacity is relatively low for Cases 1 and 2, showing rapid capacity fading. For the higher rGO concentration of 5.5 wt.% of Case 3, the initial specific capacity is the highest among the four cases, but the capacity is not maintained over 100 cycles. Even though addition of rGO accommodated volume expansion, which resulted in superior capacity initially, as observed in the SEM images, some of the Fe_2O_3 particles were supported by rGO and were not completely wrapped; thus, the exposed particles underwent pulverization during cycling, similar to Case 1 and 2. At currents of 100, 200, 500, and 1000 mA g^{-1} , the specific capacities were 1325, 1200, 1100, and 900 mAh g^{-1} respectively. However, a continuous decrease in capacity was observed up to 100 charge–discharge cycles. For Case

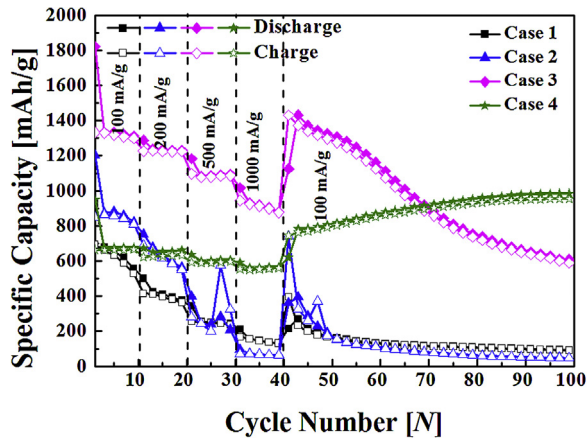


Fig. 7. Rate capability over voltage range of 0.01–3.0 V.

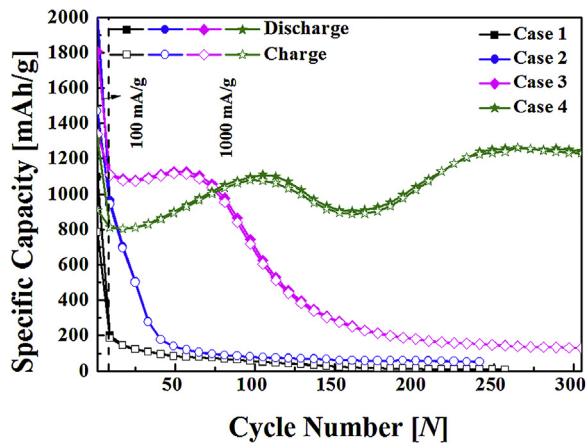


Fig. 8. Long-term cyclic performance at 1000 mA g⁻¹.

4, the capacity was initially moderate, but increased after cycling. The **Case 4** electrode showed little change in capacity with increased current, demonstrating the improved rate capability provided by the addition of conductive rGO. When the current was again reduced to 100 mA g⁻¹ at $N=40$, the original capacity at $N=1$ was not only recovered, but increased beyond the original value. Capacity increased from 800 mAh g⁻¹ at $N=41$ to 1000 mAh g⁻¹ at $N=100$, with a coulombic efficiency of 97%, demonstrating excellent lithium storage performance. The rGO-wrapped Fe₂O₃ particles underwent transformation without disrupting the electrode structure. This is due to shielding of rGO, ultimately

providing a large number of storage sites for lithium. An analogous finding has been reported by Long and coworkers [34,35]. This “comeback” behavior of the rGO-Fe₂O₃ composite is explained by activation of Fe₂O₃, which increases the active surface area by forming smaller domains of Fe₂O₃ within the rGO shield. The mechanism underlying the increased capacity has been reported to involve continuous formation of a gel-like SEI layer on the electrode surface. This SEI layer facilitates ion transport and affords excess lithium ion storage sites via “pseudocapacitance-type” behavior [36]. Cui et al. [32] documented similar results, reporting that the capacitance derived from electron double layer formation can account for the increase in the specific capacity during long-term cycling.

The long-term cycling stability of the Fe₂O₃/rGO electrodes was also evaluated at a high current density of 1000 mA g⁻¹, as shown in Fig. 8. A lower current density (100 mA g⁻¹) was used for the first 5 cycles to stabilize the performance of the cells. **Case 3** initially showed high capacity, but capacity fade was observed after 75 cycles. The initial high capacity (exceeding the theoretical capacity of Fe₂O₃) may be due to consumption of the electrolyte, which finally resulted in decreased capacity. The lower capacity observed for **Case 3** and **Case 4** in the initial high current stage may be due to concentration polarization of Li ions in Fe₂O₃, resulting from slower diffusion that also induces larger strain [11]. The capacity rise in **Case 4** is attributed to activation of Fe₂O₃ [37]. Along with an increase in the number of active sites, SEI layer formation may lower the Li ion transfer, consequently lowering the capacity observed between 125–200 cycles. However, further cycling again activates Fe₂O₃, increasing capacity. Capacity of 1242 mAh g⁻¹ was obtained after 305 cycles at a current density of 1000 mA g⁻¹. A stable SEI layer formed, as evident in Fig. S5, which demonstrates the excellent cycling stability of **Case 4**. The coulombic efficiency was >97% for **Case 4** after the first 3 cycles. Coulombic efficiency was lower for **Case 1** and **Case 2**, with dramatic capacity fade after 10 and 30 cycles, respectively, due to the large volume change and pulverization, which was evidenced in Fig. S5. Xiao et al. reported a similar trend in the case of Fe₂O₃/rGO composites fabricated via a PVP (polyvinylpyrrolidone)-assisted hydrothermal method [38]. Clearly, rGO results in better structural stability and superior cyclic performance. The use of rGO increases the overall electronic conductivity of coatings and reduces diffusion lengths for Li⁺ ions, which is also confirmed by electrochemical impedance spectra shown in supplementary Fig. S6. Furthermore, the well-dispersed Fe₂O₃ crystals incorporated into rGO can accommodate the volume change caused by lithium insertion and de-insertion. Compared with published capacity data for the Fe₂O₃ carbon composites, as presented in Table 2, the present results obtained here are quite promising.

Table 2

Comparison of specific capacities of Fe₂O₃ composites with present study.

Composition	Electrode prepared	First Discharge capacity [mAh g ⁻¹]	First reversible capacity [mAh g ⁻¹]	Reversible capacity (N th) [mAh g ⁻¹]	Current rate [mA g ⁻¹]	Refs.
Fe ₂ O ₃ /CNT	CVD	1532.3	985.8	932 (48)	Different rate	[2]
		–	–	375 (800)	3000	
Fe ₂ O ₃ /graphene/CNT	Vacuum filtration	1657	1011	716(120)	50	[39]
Carbon/Fe ₂ O ₃ /carbon	Solution method	1200	990	1087(150)	100	[36]
Fe ₂ O ₃ /graphene	Hydrothermal	1600	1150	1134(35)	100	[40]
		1180	800	1002(175)	500	
Fe ₂ O ₃ /graphene	Hydrothermal	1450	1000	1160 (100)	200	[32]
		1780	1050	838(300)	1000	
Fe ₂ O ₃ /carbon	Spray pyrolysis	1500	1020	1180(100)	100	[34]
Fe ₂ O ₃ /graphene	Hydrothermal	1554	1052	1058	50	[17]
Fe ₂ O ₃ /graphene	Sol-gel	1775	1220	1180(60)	100	[14]
Fe₂O₃/graphene	Cold spray	1300	1000	1242 (305)	1000	Present

4. Conclusions

Electrochemical measurements showed that Fe₂O₃/rGO anodes fabricated by supersonic cold spraying can exhibit high capacity, good rate capability, and promising cycling stability. The cold-sprayed nanocomposite anodes exhibited improved electrochemical performance compared to pure Fe₂O₃. The composites showed enhanced electrochemical performance in terms of the high capacity (1300 mAh g⁻¹ at 0.1C), enhanced rate capability, and excellent stability of 1242 mAh g⁻¹ at 1C, up to 305 cycles. The superior performance can be ascribed to the Fe₂O₃/rGO nanocomposite structure that can facilitate contact between the active materials and the electrolyte, enhance Li⁺ ion and electron transport, and accommodate the volume change associated with lithiation and delithiation. This approach may open a new avenue for fabrication of LIB electrodes by the facile cold spray technique.

Acknowledgement

This research was supported by Global Frontier Program through the Global Frontier Hybrid Interface Materials (GFHIM) of the National Research Foundation of Korea (NRF) funded by the Ministry of Science, ICT & Future Planning (2013M3A6B1078879) and the Industrial Strategic Technology Development Program (MKE-10045221). S.S. Yoon expresses his appreciation to the Vice Deanship of Scientific Research Chairs at King Saud University. The authors are grateful for the Nyquist plot provided by Dr. Edmund Samuel in Fig. S6.

Appendix A. Supplementary data

Supplementary data associated with this article can be found, in the online version, at <http://dx.doi.org/10.1016/j.electacta.2017.01.116>.

References

- W. Liu, P. Oh, X. Liu, M.J. Lee, W. Cho, S. Chae, Y. Kim, J. Cho, Nickel-Rich Layered Lithium Transition-Metal Oxide for High-Energy Lithium-Ion Batteries, *Angew. Chem. Int. Ed.* 54 (2015) 4440–4457.
- Y. Yang, X. Fan, G. Casillas, Z. Peng, G. Ruan, G. Wang, M.J. Yacamán, J.M. Tour, Three-dimensional nanoporous Fe₂O₃/Fe₃C-graphene heterogeneous thin films for lithium-ion batteries, *ACS nano* 8 (2014) 3939–3946.
- X. Liu, W. Si, J. Zhang, X. Sun, J. Deng, S. Baunack, S. Oswald, L. Liu, C. Yan, O.G. Schmidt, Free-standing Fe₂O₃ nanomembranes enabling ultra-long cycling life and high rate capability for Li-ion batteries, *Sci. Rep.* 4 (2014) 7452.
- S.H. Yu, S.H. Lee, D.J. Lee, Y.E. Sung, T. Hyeon, Conversion Reaction-Based Oxide Nanomaterials for Lithium Ion Battery Anodes, *Small* 12 (2016) 2146–2172.
- S. Goriparti, E. Miele, F. De Angelis, E. Di Fabrizio, R. Proietti Zaccaria, C. Capiglia, Review on recent progress of nanostructured anode materials for Li-ion batteries, *J. Power Sources* 257 (2014) 421–443.
- G. Gao, Q. Zhang, X.B. Cheng, J.G. Shapter, T. Yin, R. Sun, D. Cui, Ultrafine ferromagnetic oxide nanoparticles embedded into mesoporous carbon nanotubes for lithium ion batteries, *Sci. Rep.* 5 (2015) 17553.
- Z. Wang, D. Luan, S. Madhavi, Y. Hu, X.W. Lou, Assembling carbon-coated α-Fe₂O₃ hollow nanohorns on the CNT backbone for superior lithium storage capability, *Energy Environ. Sci.* 5 (2012) 5252–5256.
- X. Huang, J. Chen, H. Yu, R. Cai, S. Peng, Q. Yan, H.H. Hng, Carbon buffered-transition metal oxidenanoparticle-graphene hybrid nanosheets as high-performance anode materials for lithium ion batteries, *J. Mater. Chem. A* 1 (2013) 6901–6907.
- K.S. Lee, S. Park, W. Lee, Y.S. Yoon, Hollow Nanobarrels of alpha-Fe₂O₃ on Reduced Graphene Oxide as High-Performance Anode for Lithium-Ion Batteries, *ACS Appl. Mater. Interfaces* 8 (2016) 2027–2034.
- W.-J. Yu, P.-X. Hou, F. Li, C. Liu, Improved electrochemical performance of Fe₂O₃ nanoparticles confined in carbon nanotubes, *J. Mater. Chem.* 22 (2012) 13756.
- Y.-M. Lin, P.R. Abel, A. Heller, C.B. Mullins, (-Fe₂O₃) Nanorods as Anode Material for Lithium Ion Batteries, *J. Phys. Chem. Lett.* 2 (2011) 2885–2891.
- C. He, S. Wu, N. Zhao, C. Shi, E. Liu, J. Li, Carbon-encapsulated Fe₂O₄ nanoparticles as a high-rate lithium ion battery anode material, *ACS nano* 7 (2013) 4459–4469.
- N. Liu, J. Shen, D. Liu, A Fe₂O₃ nanoparticle/carbon aerogel composite for use as an anode material for lithium ion batteries, *Electrochim. Acta* 97 (2013) 271–277.
- S.H. Yu, D.E. Conte, S. Baek, D.C. Lee, S.K. Park, K.J. Lee, Y. Piao, Y.E. Sung, N. Pinna, Structure-Properties Relationship in Iron Oxide-Reduced Graphene Oxide Nanostructures for Li-Ion Batteries, *Adv. Funct. Mater.* 23 (2013) 4293–4305.
- R. Wang, C. Xu, M. Du, J. Sun, L. Gao, P. Zhang, H. Yao, C. Lin, Solvothermal-induced self-assembly of Fe₂O₃/GS aerogels for high Li-storage and excellent stability, *Small* 10 (2014) 2260–2269.
- S. Liu, Z. Chen, K. Xie, Y. Li, J. Xu, C. Zheng, A facile one-step hydrothermal synthesis of (-Fe₂O₃) nanoplates imbedded in graphene networks with high-rate lithium storage and long cycle life, *J. Mater. Chem. A* 2 (2014) 13942–13948.
- L. Tian, Q. Zhuang, J. Li, C. Wu, Y. Shi, S. Sun, The production of self-assembled Fe₂O₃-graphene hybrid materials by a hydrothermal process for improved Li-cycling, *Electrochim. Acta* 65 (2012) 153–158.
- E. García-Tamayo, M. Valvo, U. Lafont, C. Locati, D. Munao, E.M. Kelder, Nanostructured Fe₂O₃ and CuO composite electrodes for Li ion batteries synthesized and deposited in one step, *J. Power Sources* 196 (2011) 6425–6432.
- S.-L. Chou, J.-Z. Wang, D. Wexler, K. Konstantinov, C. Zhong, H.-K. Liu, S.-X. Dou, High-surface-area α-Fe₂O₃/carbon nanocomposite: one-step synthesis and its highly reversible and enhanced high-rate lithium storage properties, *J. Mater. Chem.* 20 (2010) 2092.
- D.-Y. Kim, J.-J. Park, J.-G. Lee, M.F. van Hest, S.S. Yoon, Wettability and photocatalysis of CF₄ plasma etched titania films of honeycomb structure, *Ceram. Int.* 39 (2013) 9737–9742.
- D.Y. Kim, S. Sinha-Ray, J.J. Park, J.G. Lee, Y.H. Cha, S.H. Bae, J.H. Ahn, Y.C. Jung, S. M. Kim, A.L. Yarin, S.S. Yoon, Self-Healing Reduced Graphene Oxide Films by Supersonic Kinetic Spraying, *Adv. Funct. Mater.* 24 (2014) 4986–4995.
- S. Bai, S. Chen, X. Shen, G. Zhu, G. Wang, Nanocomposites of hematite (α-Fe₂O₃) nanopillars with crumpled reduced graphene oxide nanosheets as high-performance anode material for lithium-ion batteries, *RSC Advances* 2 (2012) 10977.
- W. Xiao, Z. Wang, H. Guo, X. Li, J. Wang, S. Huang, L. Gan, Fe₂O₃ particles enwrapped by graphene with excellent cyclability and rate capability as anode materials for lithium ion batteries, *Appl. Surf. Sci.* 266 (2013) 148–154.
- J.-G. Lee, D.-Y. Kim, B. Kang, D. Kim, H.-E. Song, J. Kim, W. Jung, D. Lee, S.S. Al-Deyab, S.C. James, S.S. Yoon, Nickel-copper Hybrid Electrodes Self-adhered onto A Silicon Wafer by Supersonic Cold-spray, *Acta Mater.* 93 (2015) 156–163.
- J.-G. Lee, D.-Y. Kim, M.G. Mali, S.S. Al-Deyab, M.T. Swihart, S.S. Yoon, Supersonically Blown Nylon-6 Nanofibers Entangled with Graphene Flakes for Water Purification, *Nanoscale* 7 (2015) 19027–19035.
- D.-Y. Kim, B.N. Joshi, J.-G. Lee, J.-H. Lee, J.S. Lee, Y.K. Hwang, J.-S. Chang, S. Al-Deyab, J.-C. Tan, S.S. Yoon, Supersonic cold spraying for zeolitic metal-organic framework films, *Chem. Eng. J.* 295 (2016) 49–56.
- D.-Y. Kim, J.-G. Lee, B. Joshi, J.-H. Lee, S.S. Al-Deyab, H.G. Yoon, D.R. Yang, A. Yarin, S.S. Yoon, Supersonically sprayed thermal barrier layers using clay micro-particles, *Appl. Clay Sci.* 120 (2016) 142–146.
- A. Ferrari, J. Meyer, V. Scardaci, C. Casiraghi, M. Lazzeri, F. Mauri, S. Piscanec, D. Jiang, K. Novoselov, S. Roth, Raman spectrum of graphene and graphene layers, *Phys. Rev. Lett.* 97 (2006) 187401.
- H. Feng, X. Wang, D. Wu, Fabrication of spirocyclic phosphazene epoxy-based nanocomposites with graphene via exfoliation of graphite platelets and thermal curing for enhancement of mechanical and conductive properties, *Ind. Eng. Chem. Res.* 52 (2013) 10160–10171.
- V. Davydov, A. Rakhmanina, I. Kireev, I. Alieva, O. Zhironkina, O. Strelkova, V. Dianova, T.D. Samani, K. Mireles, L.H. Yahia, Solid state synthesis of carbon-encapsulated iron carbide nanoparticles and their interaction with living cells, *Journal of Materials Chemistry B* 2 (2014) 4250–4261.
- G.K. Pradhan, D.K. Padhi, K. Parida, Fabrication of α-Fe₂O₃ nanorod/RGO composite: a novel hybrid photocatalyst for phenol degradation, *ACS Appl. Mater. Interfaces* 5 (2013) 9101–9110.
- X. Cui, Y. Zhu, F. Li, D. Liu, J. Chen, Y. Zhang, L.L. Zhang, J. Ji, Enhanced rate capability of a lithium ion battery anode based on liquid-solid-solution assembly of Fe₂O₃ on crumpled graphene, *RSC Advances* 6 (2016) 9007–9012.
- J. Chen, L. Xu, W. Li, X.-L. Gou, α-Fe₂O₃ nanotubes in gas sensor and lithium-ion battery applications, *Adv. Mater.* 17 (2005) 582–586.
- Z. Long, L. Wei, L. Shuang, W. Jifei, W. Huanlei, C. Jiaxin, Fe₃O₄ nanoplates/carbon network synthesized by in situ pyrolysis of an organic-inorganic layered hybrid as a high-performance lithium-ion battery anode, *J. Mater. Chem. A* 3 (2015) 14210–14216.
- Y. Liu, J. Xu, X. Qin, H. Xin, X. Yuan, J. Zhang, D. Li, C. Song, Electrode activation via vesiculation: improved reversible capacity of [gamma]-Fe₂O₃/C/MWNT composite anodes for lithium-ion batteries, *J. Mater. Chem. A* 3 (2015) 9682–9688.
- Q. Qu, J. Chen, X. Li, T. Gao, J. Shao, H. Zheng, Strongly coupled 1D sandwich-like C@Fe₃O₄@C coaxial nanotubes with ultrastable and high capacity for lithium-ion batteries, *J. Mater. Chem. A* 3 (2015) 18289–18295.
- W. Sheng, G. Zhu, Q. Lu, D.L. Kaplan, Metal Oxide Nanomaterials with Nitrogen-Doped Graphene-Silk Nanofiber Complexes as Templates, Particle & Particle Systems Characterization 33 (2016) 286–292.
- L. Xiao, D. Wu, S. Han, Y. Huang, S. Li, M. He, F. Zhang, X. Feng, Self-assembled Fe₂O₃/graphene aerogel with high lithium storage performance, *ACS Appl. Mater. Interfaces* 5 (2013) 3764–3769.
- J. Wang, G. Wang, H. Wang, Flexible free-standing Fe₂O₃/graphene/carbon nanotubes hybrid films as anode materials for high performance lithium-ion batteries, *Electrochim. Acta* 182 (2015) 192–201.
- X. Meng, Y. Xu, X. Sun, J. Wang, L. Xiong, X. Du, S. Mao, Graphene oxide sheets-induced growth of nanostructured Fe₃O₄ for a high-performance anode material of lithium ion batteries, *J. Mater. Chem. A* 3 (2015) 12938–12946.